INTERNATIONAL JOURNAL FOR NUMERICAL METHODS IN ENGINEERING
Int. J. Numer. Meth. Engng 2000; **00**:1–6 *Prepared using* nmeauth.cls *[Version: 2002/09/18 v2.02]*

A Methodology for Fast Finite Element Modeling of Electrostatically-Actuated MEMS

Prasad S. Sumant [1]*, Narayana R. Aluru [1] and Andreas C. Cangellaris [2]

[1] *Dept. of Mechanical Science and Engineering, University of Illinois 1206 W. Green St., Urbana, Illinois, 61801, U.S.A.*
[2] *Dept. of Electrical and Computer Engineering, University of Illinois 1406 W. Green St., Urbana, Illinois, 61801, U.S.A.*

SUMMARY

In this paper, a methodology is proposed for expediting the coupled electro-mechanical finite element modeling of electrostatically-actuated MEMS. The proposed methodology eliminates the need for repeated finite element meshing and subsequent electrostatic modeling of the device during mechanical deformation. We achieve this by defining an auxiliary boundary value problem that involves the device geometry in the absence of actuation with modified boundary conditions for the electrostatic potential. The modification in the boundary conditions is such that the solution of the auxiliary problem for the electrostatic pressure on the movable electrode matches closely the one obtained from the solution for the electrostatic potential in the deformed geometry during actuation. The proposed methodology is demonstrated through its application to the modeling of four MEMS devices with varying length-to-gap ratios, multiple dielectrics and complicated geometries. The accuracy of the proposed methodology is confirmed through comparisons of its results with results obtained using both analytical solutions and finite element solutions obtained using ANSYS. Copyright © 2000 John Wiley & Sons, Ltd.

KEY WORDS: MEMS; modeling ; FEM; electrostatically actuated

1. INTRODUCTION

Micro-Electro-Mechanical (MEM) devices like switches, varactors and oscillators have shown great potential for use in communication devices, sensors and actuators [1]-[2]. Typically, they consist of thin, movable beams or electrodes suspended over a fixed electrode. Application of a voltage between the moveable and fixed electrodes results in electrode movement and/or deformation that can be exploited for the purposes of actuation, switching, sensing, and numerous other signal and information processing functions. In order to maximize movement while keeping the actuation voltage low, the movable beams are typically made of very thin metal films with high aspect ratios. Also, the gap between movable and fixed electrodes is

*Correspondence to: Prasad S. Sumant, Dept. of Mechanical Science and Engineering, University of Illinois 1206 W. Green St., Urbana, Illinois, 61801, U.S.A.
email: psumant2@uiuc.edu

kept sufficiently small to provide for large electrostatic forces under low actuation voltages. Multiple layers of insulating dielectric may be incorporated in the space between the electrodes to enhance performance and improve device reliability. Long-term device reliability is further enhanced through the incorporation of special features in the geometry of the electrodes, such as holes or protrusions.

The widespread insertion of MEMS devices in integrated electronics is critically dependent on the availability of accurate and computationally efficient, multi-physics CAD tools in support of device design iteration, optimization and performance degradation assessment. In support of the latter, the multi-physics modeling must comprehend all mechanisms that contribute to performance degradation. For example, in the case of RF MEMS capacitive switches the impact of charge accumulation in the insulating dielectric on the performance of the switch must be accurately quantified to enable the reliable operation of the switch [3].

A detailed characterization of an electrostatically-actuated MEMS device such as the aforementioned RF MEMS capacitive switch requires the solution of a coupled electro-mechanical problem that comprehends the movable electrodes and their support if any, as well as the potentially inhomogeneous media occupying the volume between the movable and fixed electrodes. Several one dimensional models and approximate analytical expressions have been presented for calculating the electro-mechanical response of the switch [4]. There also have been some efforts towards the development of one-dimensional models for reliability analysis [5]. Such models serve as a good starting point for the design process and provide for the development of an intuitive understanding of the operation of the device. However, these methods are limited in their description of the governing physics and, hence, unable to support the modeling detail and simulation accuracy needed for design optimization and performance degradation assessment. To provide for the needed modeling rigor and solution accuracy, finite element methods (FEM), boundary elements methods (BEM), and hybrid FEM-BEM schemes are used. For example, MEMCAD [6] uses ABAQUS, a commercial FEM package for the mechanical analysis and a BEM based program FASTCAP [7] for the electrostatic analysis. In the absence of material inhomogeneity, BEM is the method of choice for the electrostatic problem, since only the surface of the conducting electrodes need be discretized. However, for devices with significant dielectric material inhomogeneity and, in general, substantial geometric complexity, an FEM solution to the electrostatic problem offers modeling versatility and formulation simplicity. To avoid the numerical error introduced by the truncation of the finite element grid for the case of unbounded geometries, hybrid formulations where an FEM model of the interior is complemented by a BEM statement on the surface used for truncating the computational domain is possible [8],[9].

For the purposes of this paper it is assumed that the material complexity of the MEMS device under consideration is such that an FEM solution of the electrostatic boundary value problem (BVP) is preferable. Apart from the discretization of the computational domain for the solution of the electrostatic BVP, there are additional computational challenges inherent to the coupled electro-mechanical analysis.

To provide a framework for their discussion, let us consider the application of an FEM model for a coupled electro-mechanical analysis of an electrostatically actuated MEMS device. In order to keep the presentation simple, it is assumed that a relaxation-based algorithm rather than a Newton method [10] is used for the coupling of the electrostatic and the mechanical domains. The relaxation-based algorithm is as follows:

Algorithm 1
Perform an electrostatic analysis in the non-deformed geometry to calculate forces for use in the mechanical domain.

Repeat the following **until** an equilibrium state is reached:

1. Do mechanical analysis (in the non-deformed geometry) to compute structural displacements.
2. Update the geometry of the movable electrode using computed displacements.
3. Compute the electric field by electrostatic analysis (deformed geometry).
4. Compute electrostatic forces on the movable membrane in the deformed configuration.
5. Transform the electrostatic forces to the original non-deformed configuration.

During each step of the relaxation-based algorithm the beam deforms modifying the electrostatic BVP domain. In the context of BEM, a Lagrangian formulation was proposed in [11] to eliminate the need for such geometry update. In the context of FEM, the geometry update necessitates a change in the mesh used for the finite element solution of the electrostatic BVP. This is depicted for the case of the cantilever beam electrode suspended over a fixed bottom electrode in Figure 1. To update the finite element mesh for the deformed geometry one approach is to treat the mesh as another elastic solid with some appropriate elastic properties, and use the deflection of the movable beam as input boundary displacements [12],[13]. Then, using a finite element solution to the elasticity problem, the new mesh is obtained as a displacement of the previous one. This process is also known as mesh updating or mesh morphing. Similar smoothing techniques are commonly found in commercial FEM software packages such as ANSYS [14]. An alternative approach is to simply re-mesh the deformed structure at each relaxation step. Both approaches contribute an undesirable overhead to the computational cost of the iterative solution.

To avoid re-meshing the Lagrangian formulation of [11],[15] could be adopted, in principle. However, a Lagrangian formulation for FEM will require information about nodal displacements at all points in the electrical mesh, which, from a computational point of view, is not very different from a mesh update. Furthermore, a mesh update using any of the above techniques would require the finite element matrix for the electrostatic BVP to be updated and factored at every relaxation step.

The methodology proposed in this paper is aimed at overcoming the aforementioned shortcomings of the FEM solution of the electrostatic BVP by eliminating the need for mesh update. The paper is organized as follows. In Section II, the proposed methodology for the solution of the electrostatic BVP without mesh updating is presented. This is followed by the demonstration of the proposed methodology in Section III through its application to the modeling of four electrostatically-actuated MEMS devices. These numerical studies provide for the validation of the proposed methodology and the assessment of its accuracy. The paper concludes with some remarks about the types of electrostatically-actuated MEMS for which the proposed methodology is most suitable for their accurate electro-mechanical analysis.

2. PROPOSED METHODOLOGY

2.1. Auxiliary Electrostatic BVP

The proposed methodology is founded on the idea that an auxiliary electrostatic BVP can be defined on the non-deformed electrode configuration, the solution of which for the electrostatic pressure on the movable electrode is approximately equal to that obtained for the electrostatic BVP in the deformed configuration. The definition of the auxiliary electrostatic BVP is presented next.

In the deformed electrode configuration the electrostatic potential, ϕ, is obtained through the solution of the following electrostatic BVP,

$$\begin{aligned} \nabla.(\epsilon\nabla\phi(\vec{r})) &= 0 \quad \vec{r} \in \Omega_d && (1)\\ \phi(\vec{r}_s) &= V_0 \quad \vec{r}_s \in \Gamma_{1d} && (2)\\ \phi(\vec{r}_s) &= 0 \quad \vec{r}_s \in \Gamma_2 && (3)\\ \frac{\partial\phi}{\partial n} &= 0 \quad \vec{r}_s \in \Gamma_3 && (4) \end{aligned}$$

where ϵ is the dielectric permittivity, Ω_d denotes the computational domain for the deformed geometry, with boundaries Γ_{1d}, Γ_2 associated with the surfaces of the electrodes, and Γ_3 the truncation boundary. Without loss of generality it is assumed that electrode 1 is the moveable electrode; hence, the use of the subscript d in the definition of the boundary associated with its surface, to remind us that one of the electrodes for this electrostatic problem is considered in its deformed state. For our purposes it is assumed that the truncation boundary is placed at a sufficient distance from the electrodes for the amount of electric flux exiting the computational domain Ω_d to be negligible; hence, the assignment of a zero flux density condition on Γ_3. The coupling between the mechanical and electrical domains happens through the electrostatic pressure, P, on the movable electrode. It is given by,

$$P = \frac{{\rho_s}^2}{2\epsilon} \tag{5}$$

where the electric charge density on the conductor surface is given by

$$\rho_s = \hat{n} \cdot (-\epsilon\nabla\phi) \tag{6}$$

In the above equation $\hat{n}$ is the outward pointing unit normal on the conductor surface. Since on a conducting surface the electric field intensity $\vec{E} = -\nabla\phi$ has only the normal component, the electrostatic pressure on the movable electrode is cast in the following form

$$P = \frac{1}{2}\epsilon \left|\nabla\phi\right|^2 \tag{7}$$

We propose the following auxiliary electrostatic BVP on the non-deformed domain Ω_0.

$$\begin{aligned} \nabla.(\epsilon\nabla\phi(\vec{r})) &= 0 \quad \vec{r} \in \Omega_0 && (8)\\ \phi(\vec{r}_s) &= V(\vec{r_s}) \quad \vec{r}_s \in \Gamma_1 && (9)\\ \phi(\vec{r}_s) &= 0 \quad \vec{r}_s \in \Gamma_2 && (10)\\ \frac{\partial\phi}{\partial n} &= 0 \quad \vec{r}_s \in \Gamma_3 && (11) \end{aligned}$$

A few comments are in order with regards to the above statement of the auxiliary BVP. First of all, we note that Γ_1 is the surface of the movable electrode 1 in the absence of actuation and, hence, in its non-deformed state. More importantly, for the purposes of the auxiliary BVP, the surface Γ_1 is no longer considered an equipotential surface. Rather, it is taken to be a mathematical surface on which the assigned potential value is position dependent. In particular, the choice of $V(\vec{r})$ should be such that the solution of the auxiliary BVP yields closely the same electrostatic pressure on the movable electrode as that obtained through the solution of the electrostatic BVP in the deformed configuration.

To elucidate this point, we consider the simple configuration of a cantilever beam suspended over a ground plane. Without loss of generality and for the sake of simplicity of the following discussion, it is assumed that the medium between the electrodes is homogeneous of constant permittivity, ϵ. The electrode thickness is assumed to be negligible. Furthermore, as is commonly the case in electrostatically-actuated MEMS, the distance between the electrodes is assumed to be much smaller than their lengths. Thus, fringing fields at the edges are negligible, with most of the electric flux present inside the volume between the electrodes.

At an intermediate step in the relaxation algorithm for the solution of the electro-mechanical problem the cantilever beam is bent in a position as shown in Figure 2(a). This constitutes the deformed configuration. The corresponding non-deformed configuration in which the auxiliary electrostatic BVP is defined is depicted in Figure 2(b). In the non-deformed configuration the movable electrode boundary is replaced by a mathematical surface, S_f, on which a position-dependent potential is assigned.

In the deformed configuration the line integral of the electric field along the path of a flux line from one electrode to the other is constant and equal to the potential difference between the electrodes. Next we consider the extension of an electric flux line path from the top electrode in the deformed configuration along the direction perpendicular to the electrode and until it intersects S_f at a point of coordinate x. Under the assumption of small displacements, the value of the electric flux density along this extension of the electric flux line is taken to be equal to its value right at the electrode. Then the voltage at point x on S_f is given by

$$V(x) \approx V_0 + E(x)L_1(x) \tag{12}$$

where $L_1(x)$ is the length of the path from the top electrode to S_f and $E(x)$ is the electric field intensity at the electrode. Since the electric flux density is constant along the electric flux line between the two electrodes, it is

$$E(x) = \frac{V_0}{L_2(x)} \tag{13}$$

where $L_2(x)$ is the length of the path between the two electrodes along the flux line. Combining the last two equations we obtain

$$V(x) \approx V_0 \frac{L_1(x) + L_2(x)}{L_2(x)} \tag{14}$$

This result suggests that the definition of the position-dependent voltage along the mathematical surface S_f is possible provided that the lengths $L_1(x)$ and $L_2(x)$ can be computed.

Before we proceed with the presentation of two methods for the approximate computation of $L_1(x)$ and $L_2(x)$ we would like to point out that the electric field $E(x)$ at position x along

the mathematical surface S_f (see Figure 2) is not perpendicular to the surface. Its direction is along the electric flux line that was extended, in the direction perpendicular to the surface of the deformed electrode until it interested S_f at position x. Under the assumption of small displacement of the moving electrode, this ensures, with very good accuracy, the equality between the net electric flux through the top electrode in its deformed position with the net electric flux through the surface S_f. Furthermore, it suggests that, the calculated electrostatic pressure on S_f at position x will be in the direction of $E(x)$ or, equivalently, in the direction of the extended flux line from the deformed electrode that intersects S_f at position x.

Next, we proceed with the proposition of two methods for the approximate computation of $L_1(x)$ and $L_2(x)$.

2.2. Method 1: Using geometry

This method exploits the fact that for most electrostatically-actuated MEMS devices the lengths of the electrodes are much larger than both the thickness of the electrodes and their separation. For example, length to separation ratios of values ranging between 50:1 to 200:1 are very common in practical devices. With this in mind, the following equations are proposed for the approximation of the lengths $L_1(x)$ and $L_2(x)$:

$$L_1(x) = v(x) \tag{15}$$

$$L_2(x) = G - v(x) \tag{16}$$

$$L_1(x) + L_2(x) = G \tag{17}$$

where G is the distance between the movable and fixed electrodes in the absence of actuation, while $v(x)$ is the displacement of the movable electrode at position x along its axis. Thus, (14) can be written as

$$V(x) \approx V_0 \frac{G}{G - v(x)} \tag{18}$$

Clearly, the above choice is based on the assumption that, with both electrodes fixed at their rest position, the length of every flux line starting from one electrode and terminating on the other is approximately constant and is equal to the physical separation between the electrodes in the absence of actuation. As it will be demonstrated through the numerical studies in Section III, this method works very well for geometries consisting of cantilever or simply supported beams, especially for devices with electrodes of comparable lengths, where the definition of an electrode-to-electrode separation G is straightforward from the device geometry. However, there are classes of MEMS devices, such as comb drives and other structures with electrodes of disparate lengths and shapes, where the definition of an electrode-to-electrode separation distance G is more cumbersome or even impossible. To provide for a fully automated process for the approximation of the lengths $L_1(x)$ and $L_2(x)$, the following method is proposed.

2.3. Method 2: Using Electric field distribution

This method is prompted by the observation that for the case of devices exhibiting asymmetry in their electrode shapes, lengths and placement, the total length of an electric flux line starting from one electrode and ending on the other will be position dependent. Thus, a position-dependent separation function, $G(x)$, should be defined, understood as the length of different

electric flux lines between the electrodes. To provide for the calculation of such a position-dependent separation distance, use is made of the calculated surface charge density on the moveable electrode after the first step of relaxation process. Its value at a specific point x along the electrode, divided by the permittivity of the medium between the electrodes (which, for the sake of simplicity and without loss of generality, is assumed to be constant), yields the electric field intensity value, $E(x)$, along the electric flux line path that terminates at that point. Thus, $G(x)$ is computed by

$$G(x) = \frac{V_0}{E(x)} \tag{19}$$

where V_0 is the potential difference between the electrodes. Once the $G(x)$ is available, $L_1(x)$ and $L_2(x)$ are computed from (15)-(17) with G replaced by $G(x)$.

The example geometry of a cantilever beam suspended over a ground electrode of different length, as depicted in Figure 3, helps demonstrate the way $G(x)$ is computed through the aforementioned methodology. From the computed electric field intensity values along the top movable electrode, it is clear that its value is maximum over the portion of the movable electrode directly above the bottom electrode. The field intensity decays rapidly as we move away from and to the left of the left edge of the bottom electrode. Incorporating this variation in the computation of a position-dependent $G(x)$ results in the distribution depicted in the bottom plot of Figure 3.

It is evident from the plot that $G(x)$ remains constant and equal to the physical separation between the two electrodes over the right-end portion of the top beam, which is located above the bottom electrode. As we approach the edge of the bottom electrode $G(x)$ starts increasing, eventually assuming very large values at distances sufficiently far away from the left edge of the bottom electrode. From (18) it is apparent that a large value of $G(x)$ indicates that $V(x)$ is insensitive to the displacement of the top electrode far away from the left edge of the top electrode. This is consistent with the governing physics, since the portion of the beam away from the left edge of the bottom electrode experiences very small displacement. On the other hand, since the $G(x)$ equals the physical separation between the two electrodes over the segment of the top beam directly above the bottom electrode, it captures the displacement of the beam very effectively.

Also, note that the electric field intensity is bound to exhibit very large values at the edges of the conducting electrodes, as the numerical solution attempts to reproduce the charge density singularity in the neighborhood of the edges. In these cases, $G(x)$ may assume values much smaller than the value of the physical separation between the two electrodes. To avoid numerical difficulties due to such behavior, we impose a condition that

$$G(x) \geq G \tag{20}$$

With either one of the aforementioned methods used for the computation of the lengths $L_1(x)$ and $L_2(x)$, the auxiliary electrostatic BVP may be cast in the form:

$$\nabla.(\epsilon\nabla\phi(\vec{r})) = 0 \qquad \vec{r} \in \Omega_0 \tag{21}$$

$$\phi(\vec{r}_s) = V_0 \frac{G(\vec{r}_s)}{G(\vec{r}_s) - v(\vec{r}_s)} \quad \vec{r}_s \in \Gamma_1 \tag{22}$$

$$\phi(\vec{r}_s) = 0 \qquad \vec{r}_s \in \Gamma_2 \tag{23}$$

$$\frac{\partial\phi}{\partial n} = 0 \qquad \vec{r}_s \in \Gamma_3 \tag{24}$$

The algorithm for performing the FEM-based electro-mechanical analysis utilizing the aforementioned approach is as follows:
Algorithm 2

1. Solve the auxiliary electrostatic FEM problem with constant potential V_0 on Γ_1.
2. Using the computed electric field intensity distribution on Γ_1, compute $G(\vec{r}_s)$ for Method 2. For Method 1, skip this step.
3. Loads/boundary conditions for the mechanical solution are computed using the calculated values of the electric field and its direction along the movable electrode.
4. Solve the mechanical FEM to compute the deflection/deformation of the movable electrode.
5. Using the calculated displacement $v(\vec{r}_s)$ of the movable electrode, update the potential along Γ_1 using (eqn(22)). The electrical mesh remains the same, only the dirichlet boundary conditions are modified.
6. Go to step 3 and repeat until convergence

Clearly, since the geometry in the auxiliary electrostatic BVP does not change, there is no need for re-meshing and re-generating the FEM matrix for the electrostatic BVP. Thus, in subsequent steps, the same factorization of the electrostatic FEM matrix can be used. This results in computation savings at every relaxation step.

2.4. Physical Interpretation of $G(x)$ for inhomogeneous dielectrics

In this section, we provide a physical interpretation of $G(x)$ in the presence of an inhomogeneous dielectric medium between the electrodes. For the purpose of illustration, let us consider the geometry as depicted in Figure 4. Let V_0 be the potential difference between the two electrodes. The electric permittivity of the insulating material is assumed position dependent. Also, shown in the figure is a flux line C between the two electrodes. Along such a flux line the magnitude of the electric flux density $\vec{D}_c$ is constant. Hence, we can write,

$$\int_C \vec{E}.\vec{dl} = V_0 \tag{25}$$

$$\int_C \frac{\vec{D}_c.\vec{dl}}{\epsilon(\vec{r})} = V_0 \tag{26}$$

$$\int_C \frac{1}{\epsilon(\vec{r})} dl = \frac{V_0}{\left|\vec{D}_c\right|} \tag{27}$$

Let $\vec{E}(x_c)$ be the electric field at the point on the electrode on the flux line C and let $\epsilon(x_c)$ be the electric permittivity in the medium right next to that point. Then we can write

$$\vec{D_c} = \epsilon(x_c)\vec{E}(x_c) \tag{28}$$

$$\int_C \frac{\epsilon(x_c)}{\epsilon(\vec{r})} dl = \frac{V_0}{\left|\vec{E}(x_c)\right|} \tag{29}$$

$$G(x_c) = \int_C \frac{\epsilon(x_c)}{\epsilon(\vec{r})} dl = \frac{V_0}{\left|\vec{E}(x_c)\right|} \tag{30}$$

This relationship thus defines an *effective gap length* between the two electrodes in the presence of an inhomogeneous dielectric medium. This relationship is the same as eqn(19). Thus, this approach of defining $G(x)$ is very general and takes care of the presence of inhomogeneous dielectrics.

2.5. Computational complexity analysis

In the following we compare the computational complexity of the two algorithms, Algorithm 1 of Section I used in the standard FEM electro-mechanical analysis, and Algorithm 2, resulting from the implementation of the methodology proposed in this paper for the FEM solution of the electrostatic BVP. For this purpose, the following notation will be used:

- N_m: number of nodes in the FEM mesh for the mechanical problem
- N_e: number of nodes in the FEM mesh for the electrostatic problem
- N_i: number of nodes at the boundary of the movable electrode for the mechanical problem and on S_f for the auxiliary electrostatic problem
- N_{iter}: number of relaxation steps for convergence

Table I summarizes the comparison of the two algorithms. An explanation of the entries in Table I is as follows. For both the algorithms, the stiffness matrix for the mechanical domain needs to be assembled and factored only once. The FEM system for the mechanical domain needs to be solved at every relaxation step for both algorithms. For Algorithm 1, the stiffness matrix for the electrostatic problem needs to be reassembled and factored at every relaxation step as the geometry of the electrostatic problem changes at every step due to electrode deformation. In contrast, in Algorithm 2, this has to be done only once, since the deformed geometry is reflected only in an updated boundary condition for the electrostatic potential on the fixed surface S_f. Furthermore, in Algorithm 1, an FEM mesh update is required at every relaxation step. This cost is completely eliminated in Algorithm 2.

Assuming $N_{iter} = 10$, the computational cost for each algorithm is obtained from the entries of Table I, as follows:

$$\begin{aligned} \textit{Algorithm } 1: \quad & O(N_m^{1.5} + 13N_e^{1.5} + 11N_m + 42N_e + 20N_i) \\ & \approx O(N_m^{1.5} + 13N_e^{1.5}) \end{aligned} \tag{31}$$

$$\begin{aligned} \textit{Algorithm } 2: \quad & O(N_m^{1.5} + N_e^{1.5} + 11N_m + 11N_e + 20N_i) \\ & \approx O(N_m^{1.5} + N_e^{1.5}) \end{aligned} \tag{32}$$

Thus Algorithm 2, based on the proposed methodology, is roughly 10 times more efficient than Algorithm 1.

3. NUMERICAL STUDIES

Four case studies are presented next for assessing the performance and demonstrating the accuracy and versatility of the proposed method. These studies involve some of the most common electrode geometries used in electrostatically-actuated MEMS devices. Each individual case study presents some unique challenges that, as it will be demonstrated, are successfully handled by the proposed method.

3.1. Cantilever series switch

One of the most important RF MEMS switches is the cantilever series switch [4] depicted in Figure 5(a). It consists of a beam suspended over a bottom ground electrode, which is part of a microwave, planar transmission line. The bottom ground electrode is on top of a silicon substrate. The purpose of this case study is to demonstrate the applicability and accuracy of the proposed method for handling cantilever geometries with asymmetric placement of electrodes.

The modeled geometry is depicted in Figure 5(b). Note that the silicon substrate is not included in this study. The top electrode is 150 μm in length, 2 μm in thickness. The Young's modulus E is 170 GPa and the Poisson's ratio ν is 0.34. The bottom electrode is 50 μm in length, 2 μm in thickness, and located 100 μm from the leftmost end of the top electrode. The structure was analyzed for different values of the gap length, ranging from 1.5 μm to 4.5 μm. Thus, the length to gap ratio (for the top electrode) is varied between 100:1 to 33.33:1. This is done to demonstrate the robustness and accuracy of the proposed approach for varying length to gap ratios. Recall that in most practical applications, the length to gap ratio is kept as high as possible, with length to gap ratios between 50:1 to 100:1 being the most common.

Four-node quad elements are used for the mechanical mesh whereas three-node triangles are used for the electrical mesh. ESSOLV macro in ANSYS, which is a sequential coupled field solver, is used for the implementation of Algorithm 1 and for providing the reference solution. For each value of the length of the gap, the applied voltage is varied up to its pull-in value. Figures 6-7 depict the computed deflections for four different values of gap length. The proposed methodology is seen to be accurate up to pull in, for both Methods 1 and 2 for the computation of the lengths $L_1(x)$ and $L_2(x)$. The difference with the ANSYS result increases slightly as the applied voltage approaches its pull-in value. However, the results obtained using the proposed methodology remain within 2-3 % of the ANSYS results. Table II compares the pull-in voltages obtained using ANSYS (Algorithm 1) and the proposed methodology (Algorithm 2) for different gap lengths. Good agreement is observed.

3.2. Simply-supported RF MEMS capacitive switch

The MEMS device under study in this section is the simply-supported RF capacitive switch of [16], depicted in Figure 8. It consists of a Au beam for the top movable electrode, suspended over a center ground conductor, which is part of a coplanar waveguide. The center ground electrode is placed on top of a SiO_2 layer, which is on top of a silicon substrate. A thin layer of silicon nitride is deposited on top of the center conductor. This layer of dielectric prevents direct metal to metal contact of the two electrodes. The presence of the metal posts at which the top beam is attached provide for a natural truncation of the computational domain on the two sides and the top. A truncation boundary is introduced in the Si substrate, resulting in

the cross-sectional geometry of the computational domain depicted in Figure 8.

Since the width of the top electrode is much larger than the vertical thickness, a two-dimensional analysis, involving the cross-sectional geometry depicted in Figure 8 suffices. The geometric dimensions that define the cross-sectional geometry are as follows. The length of the top electrode is 300μm. Its thickness, t, is 0.8μm. The length of the lower electrode is 100 μm and its thickness, t_e, is 0.8μm. The silicon oxide layer thickness, t_{ox}, is 0.4 μm. The silicon nitride thickness, t_d, is 0.15 μm. The relative permittivities of the Si_3N_4 and SiO_2 layers, are, respectively, 7.6 and 3.9 . The relative permittivity of Si is taken to be 11.7. For the Au beam, the Young's modulus, E, is 80 GPa and the Poisson's ratio ν is 0.42. The thickness of the Si layer is 30 μm. The boundary condition imposed at the bottom truncation boundary for the electrostatic BVP is one of zero electric flux density.

Like in the previous case, we consider designs with different gap lengths, g_0. The ESSOLV macro in ANSYS is used for generating the reference solution, based on the application of Algorithm 1. For each value of the length of the gap, the applied voltage is varied up to its pull-in value. Figures 9-10 depict the computed deflections for four different values of gap length. The proposed methodology is seen to be very accurate up to pull in, for both Methods 1 and 2 for the computation of the lengths $L_1(x)$ and $L_2(x)$. The difference with the ANSYS result increases slightly as the applied voltage approaches its pull-in value. However, the results obtained using the proposed methodology remain within 2-3 % of the ANSYS results.

3.3. Comb drive

Electrostatically-actuated comb drives are an important class of MEMS structures having numerous applications from micro-accelerometers and position controllers to hard disk drive actuators [17],[10],[18]. This case study considers the application of the proposed methodology to the electro-mechanical FEM modeling of the transverse comb drive depicted in Figure 11(a). The system consists of a movable center stage, 24 pairs of interdigitated teeth and four spring beams. The center stage is supported by four folded spring beams anchored at the ends. Electrostatic forces are generated when a voltage is applied between the fixed and movable structures. The movable center stage is 100 μm long, 200 μm wide and 3.7 μm thick. The small and large gaps between the two electrodes are g_1=2μm and g_2=5μm. The overlap length is 50 μm and the finger width is 4 μm. The beam width is 3 μm, and the lengths of the short and long parts of the folded beam are l_1=80μm and l_2=120μm, respectively. The Young's modulus of the comb structure is 200 GPa and the Poisson's ratio is 0.31. Due to symmetry, it is sufficient to consider the modeling of just the lower portion, depicted in Figure 11(b). The surrounding medium is assumed to be homogeneous with electric permittivity that of free space ϵ_0.

For small displacements, the displacement of the movable stage can be obtained from analytical analysis [17]

$$\frac{hl_t\epsilon}{2}\left[\frac{1}{(g_1-x)^2}-\frac{1}{(g_2+x)^2}\right]V^2 = Eh\frac{b^3}{l_1^3+l_2^3}x \tag{33}$$

where h is the thickness of the structure, x is the transverse displacement of the moving stage and V is the applied voltage. Plotted in Figure 12 is a comparison between results from the above analytical expressions and those obtained using Method 2. Application of Method 1 for this geometry, while possible, requires the a-priori identification of the fixed gap lengths for

different portions of the moving electrode. In contrast, Method 2 provides an automatic way for their computation. Thus, it is preferable for structures exhibiting substantial geometric complexity, such as in the case of a comb drive.

3.4. Torsional micro mirror

Torsional micro-mirrors have been widely used in applications such as spatial light modulators, optical crossbar switches, adaptive optics and digital projection displays [19],[20]. This case study focuses on the application of our proposed method to the electrostatic analysis of a typical torsion micro mirror device. Such a device offers unique challenges to our simulation because it involves a rotation of the electrodes and has inherent fringing effects.

Figure 13a shows the most general design of a torsion micro mirror reported in the literature [19],[21]. It consists of two metal electrodes mounted on a beam that is pivoted at the center. The beam is free to rotate about the pivot. There are two bottom electrodes located at a certain distance below the top electrodes. A voltage applied between two electrodes on one side produces an electrostatic force of attraction between them which results in a torque on the beam. This torque causes the beam to rotate and rest at an angle to the original position. The most important design parameter of a torsion micro mirror is the maximum angle it can rotate to before it snaps and pulls in. This parameter depends on the gap between the top and bottom electrodes and the length of the top beam. In literature, most length-to-gap ratios have been found to be greater than 50:1.

For the purpose of demonstrating the limits of our method, we consider a design of a micro-mirror with a length-to-gap ratio of 10:1. Note that this poses significant challenges to the simulation since it has considerable fringing effects. We consider the state of a torsion mirror just before/at pull in. So we consider the maximum rotation of the top beam. From [21], the angle α at which the beam pulls in is given by,

$$\alpha = 0.44\frac{d}{L} \tag{34}$$

where d is the distance between the top and bottom electrodes and L is the length of the beam on one side of the pivot.

We apply our proposed approach (to the undeformed configuration Figure 13a) to calculate the electric field along the top electrodes in the deformed configuration and compare it with the conventional FEM analysis for the beam in the deformed configuration (Figure 13b). The results are shown in Figure 14a. It is clear that very good agreement is observed. The charge density along the top electrode determines the electrostatic pressure (eqn (5)). Since the electric field along the top left electrode is atleast 1000 times more than that of the top right electrode, the charge density along the top right electrode is negligible. The % error in charge density along the top left electrode is plotted in Figure 14b. The maximum error is about 3 % which occurs at the extreme left. Along the beam the error is less than 1 % demonstrating the accuracy of our proposed method.

4. CONCLUSIONS

In summary, we have proposed a methodology for expediting the coupled electro-mechanical finite element modeling of electrostatically-actuated MEMS devices. The enhanced efficiency

of the proposed methodology is achieved by eliminating the mesh updating, stiffness matrix calculation, and stiffness matrix factorization, associated with the FEM solution of the electrostatic problem at each step of a relaxation-based algorithm, which is assumed to be used for the electro-mechanical simulation. The way this is accomplished is through the introduction of an auxiliary electrostatic BVP on a fixed geometry, namely, the geometry of the MEMS structure in the absence of actuation. In this auxiliary problem the movable electrodes are replaced by mathematical surfaces on which position-dependent voltages are assigned. These position-dependent boundary conditions are dependent on the electrode deformation, calculated through the solution of the mechanical problem, and are such that the solution of the auxiliary problem for the electrostatic pressure on the movable electrode matches accurately the one obtained from the solution for the electrostatic potential in the deformed geometry during actuation.

The proposed methodology was validated through its application to the modeling of four classes of MEMS geometries, namely, a cantilever series switch, a simply-supported RF MEMS capacitive switch, a transverse comb drive and a torsion micro mirror. The dimensions and material properties used for the validation studies were representative of practical MEMS devices. Through comparisons with reference solutions obtained using either FEM electro-mechanical modeling using ANSYS or analytical solutions where appropriate, it was shown that the proposed methodology is very accurate for the four classes of the small-displacement, electrostatically-actuated MEMS devices considered. This was achieved at an estimated one order-of-magnitude reduction in the computational cost compared to a standard FEM-based electro-mechanical modeling.

ACKNOWLEDGEMENTS

This research was supported in part by the Defense Advanced Research Projects Agency (DARPA), under the N/MEMS Science & Technology Fundamentals Research Program.

REFERENCES

1. Yao J. RF MEMS from a device perspective *Journal of Micromechanics and Microengineering* 2000; **10**:9–38.
2. Tillmans H, Raedt W, Beyne E. MEMS for wireless communications: 'from RF-MEMS components to RF-MEMS-SIP' *Journal of Micromechanics and Microengineering* 2003; **13** : 139–163.
3. Goldsmith C, Ehmke J, Malczewski A , Pillans B , Eshelman S, Yao Z, Brank J, Eberly M. Lifetime characterization of capacitive RF MEMS switches *IEEE MTT-S Int. Microwave Symp. Dig.* 2001; 227–230.
4. Varadan V, Vinoy K, Jose K. *RF MEMS and Their Applications*. John Wiley, 2003.
5. van Spengen W , Peurs R, Mertens R, Wolf I. A comprehensive model to predict the charging and reliability of capacitive RF MEMS switches *Journal of Micromechanics and Microengineering* 2004; **14** : 514–521.
6. Senturia S, Harris R, Johnson B, Songmin K, Nabors K, Shulman M, White J. A computer-aided design system for microelectromechanical systems (MEMCAD) *Journal of Microelectromechanical systems* 1992; **1** : 3–13.
7. Nabors K, White J. FastCap: A multi-pole accelerated 3-D capacitance extraction program *IEEE Trans. Comput.-Aided Design* 1991; **10** : 1447–1459.
8. Jin J. *The Finite Element Method in Electromagnetics*. John Wiley, 2002.
9. Li G , Aluru N. *Hybrid techniques for electrostatic analysis of nanoelectromechanical systems Journal of Applied Physics* 2004; **96** : 2221–2231.

10. De S, Aluru N. Full-Lagrangian Schemes for Dynamic Analysis of Electrostatic MEMS *Journal of Microelectromechanical systems* 2004; **13**: 737–758.
11. Li G, Aluru N. A Lagrangian Approach for Electrostatic Analysis of Deformable Conductors *Journal of Microelectromechanical systems* 2002; **11** : 245–254.
12. Soma A, Bona F, Gugliotta A, Mola E. Meshing approach in non-linear FEM analysis of microstructures under electrostatic loads *Proceedings of SPIE* 2001; **4408** : 216–225.
13. Chiandussi G, Bugeda G, Onate E. A simple method for automatic update of finite element meshes *Communications in Numerical Methods in Engineering* 2000; **16** : 1–19.
14. Zhulin V, Owen S, Ostergaard D. Finite Element Based Electrostatic-Structural Coupled Analysis with Automated Mesh Morphing *International Conference on Modeling and Simulation of Microsystems* 2000; 501–504.
15. Telukanta S, Mukherjee S. Fully Lagrangian Modeling of MEMS with thin plates *Journal of Microelectromechanical systems* 2006; **15**(4) : 795–810.
16. Hamad E, Omar A. An improved two-dimensional coupled electrostatic-mechanical model for RF MEMS switches *Journal of Micromechanics and Microengineering* 2006; **16** : 1424–1429.
17. Imamura T, Katayama M, Ikegawa Y, Ohwe T, Koishi R, Koshikawa T. MEMS-based integrated head/actuator/slider for hard disk drives *IEEE/ASME Trans.Mechatron* 1998; **3** : 167–174.
18. Ye W, Mukherjee S. Optimal shape design of three-dimensional MEMS with applications to electrostatic comb drives *International Journal for Numerical Methods in Engineering* 1999; **45** : 175–194.
19. Zhang X, Chau F, Quan C, Lam Y, Liu A. A study of the static characteristics of a torsion micromirror *Sensors and Actuators A* 2001; **90** : 73–81.
20. Buhler J, Funk J, Korvink J, Steiner F, Sarro P, Baltes H. Electrostatic Aluminum micromirrors using double-pass metallization *Journal of Microelectromechanical systems* 1997;**6**(2):126–135.
21. Degani O, Socher E, Lipson A, Leitner T, Setter D, Kaldor S, Nemirovsky Y. Pull-In Study of an Electrostatic Torsion Microactuator *Journal of Microelectromechanical systems* 1998;**7**(4):373–379.

Table I. Computational complexity of Algorithm 1 and Algorithm 2

step	order	Algorithm 1	Algorithm 2
Assembly			
Stiffness matrix for mechanical domain	N_m	1	1
Stiffness matrix for electrical domain	N_e	N_{iter}	1
Stiffness matrix for pseudo-elastic (electrical) domain	$2N_e$	1	0
Factorization of stiffness matrix			
Stiffness matrix for mechanical domain	$N_m^{1.5}$	1	1
Stiffness matrix for electrical domain	$N_e^{1.5}$	N_{iter}	1
Stiffness matrix for pseudo-elastic (electrical) domain	$(2N_e)^{1.5}$	1	0
Forward and backward solve for linear system			
for mechanical domain	N_m	N_{iter}	N_{iter}
for electrical domain	N_e	N_{iter}	N_{iter}
for pseudo-elastic (electrical) domain	$(2N_e)$	N_{iter}	0
Update interface conditions			
to calculate electrostatic forces for mechanical domain	N_i	N_{iter}	N_{iter}
to calculate mechanical displacements for electrical domain	N_i	0	N_{iter}
to calculate mechanical displacements for pseudo-elastic domain	N_i	N_{iter}	0

Table II. Variation of pull-in voltage with gap

	Pull in voltage (V)		
Gap(μm)	ANSYS	Method 1	Method 2
1.5	21	21	20
2.0	31	30	31
3.0	58	57	57
4.5	105	101.5	101.5

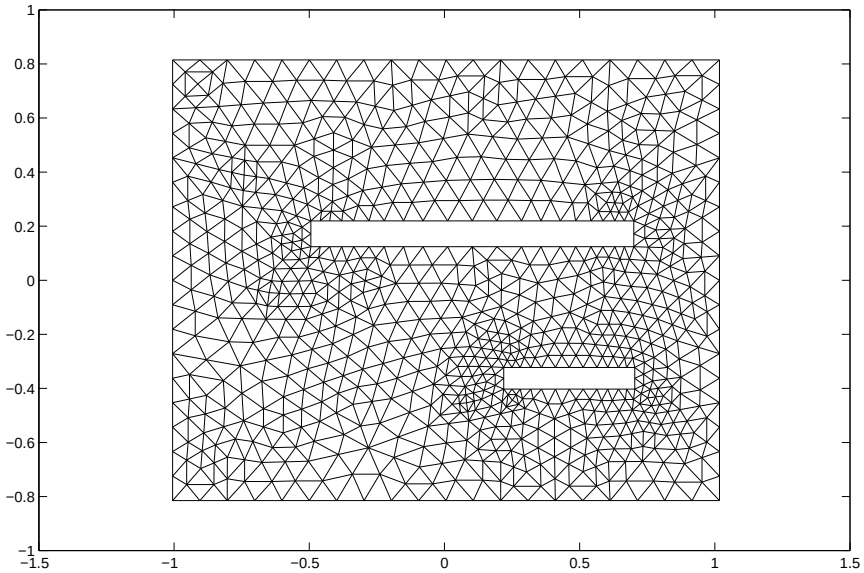

(a)

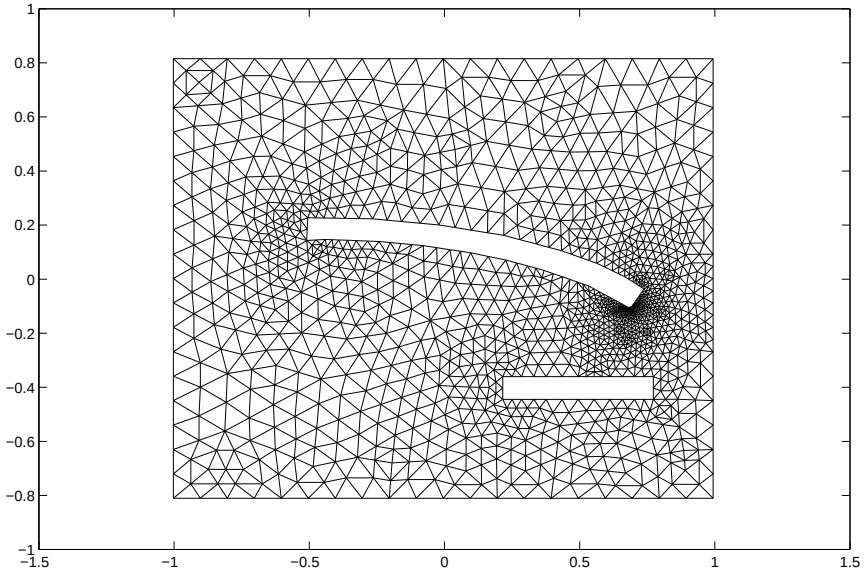

(b)

Figure 1. Conventional FEM electro-mechanical modeling: (a) Electrostatic BVP meshing of non-deformed configuration (b) Electrostatic BVP meshing of deformed configuration

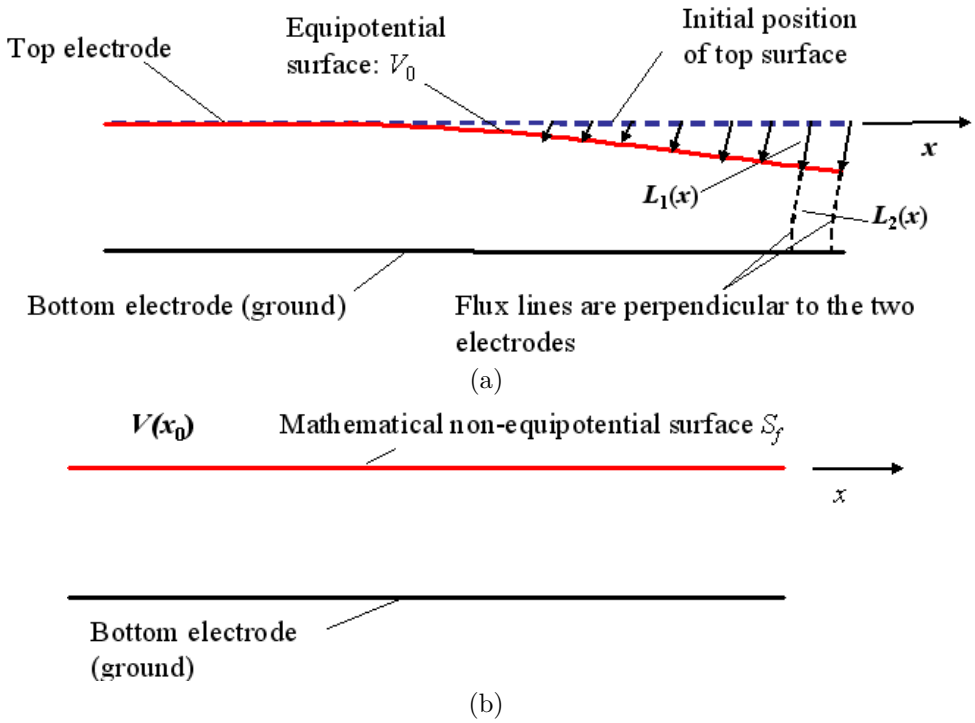

Figure 2. Proposed Approach : Mapping (a) Deformed configuration to (b) Non-deformed configuration

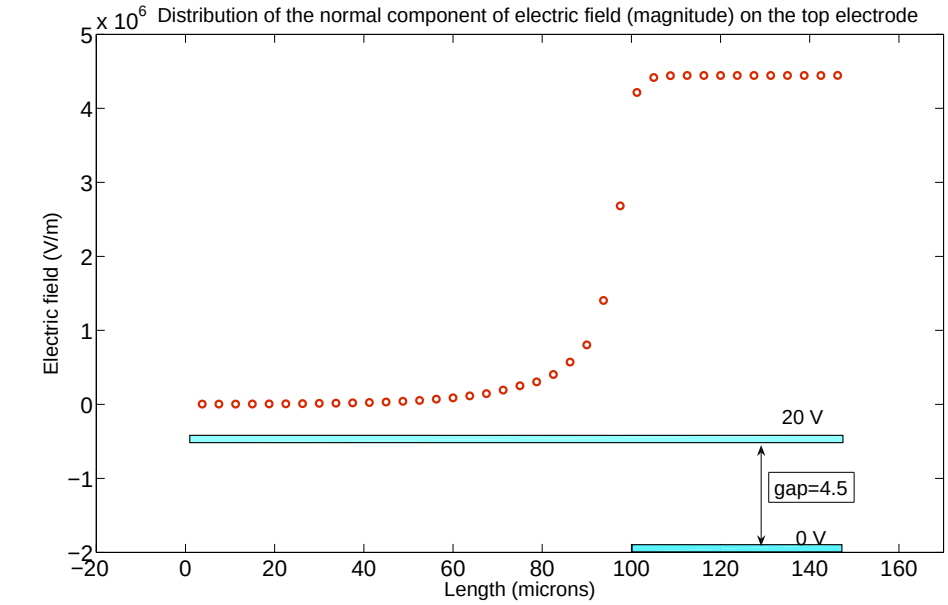

(a)

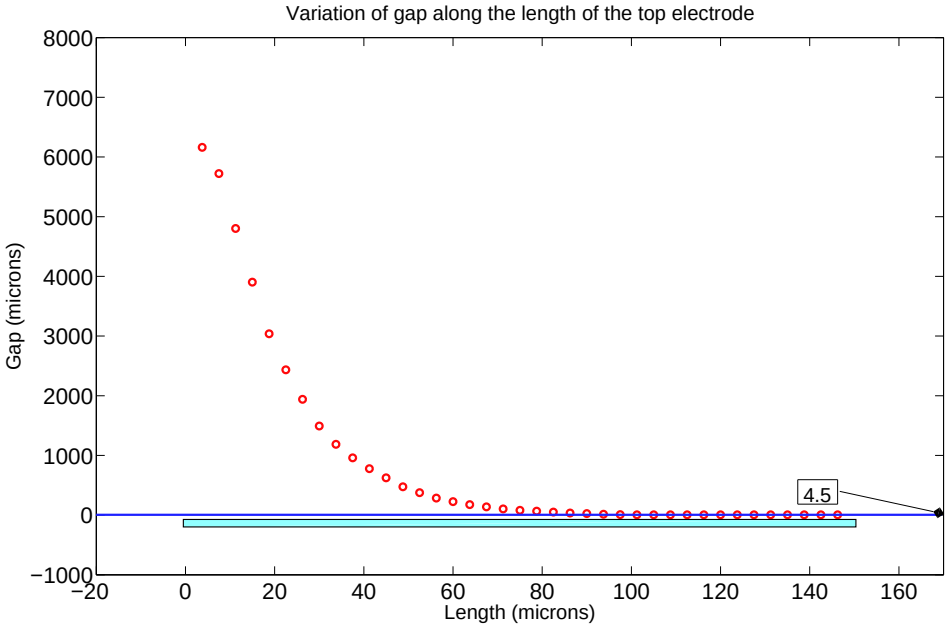

(b)

Figure 3. $G(x)$ calculation using electric field distribution. (a) Electric field distribution (b) Position-dependent electrode separation $G(x)$

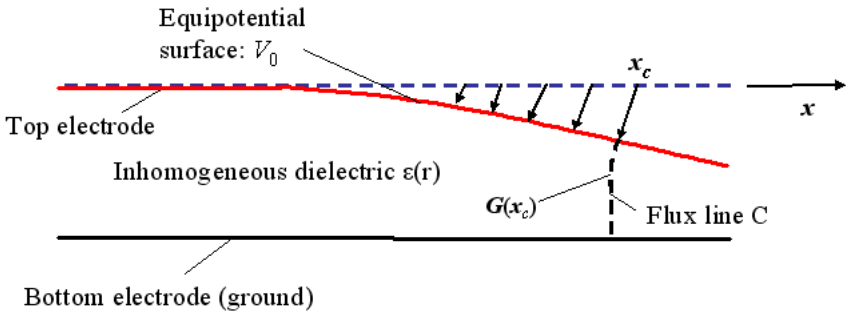

Figure 4. Physical interpretation of $G(x)$ calculation using electric field distribution.

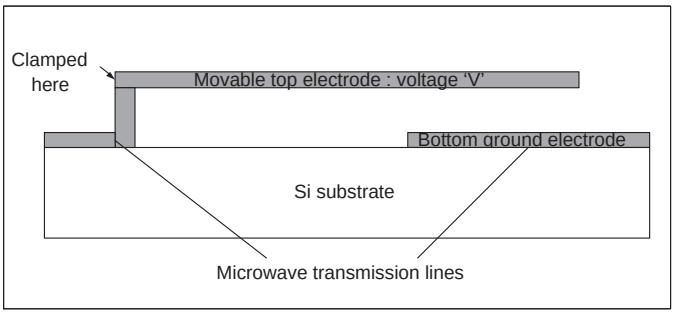

(a)

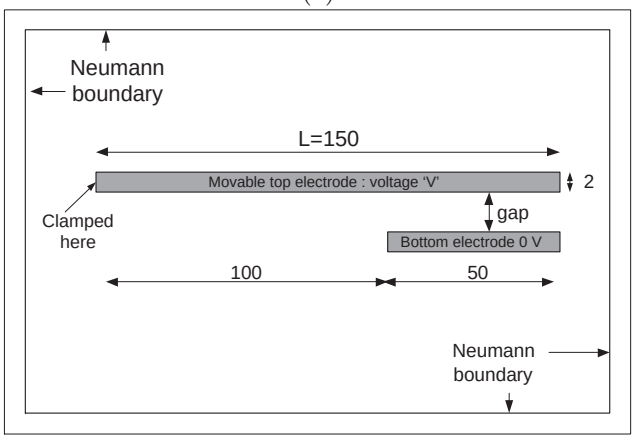

(b)

Figure 5. Cantilever series switch (a) Actual device (b) Modeled geometry. All dimensions in microns.

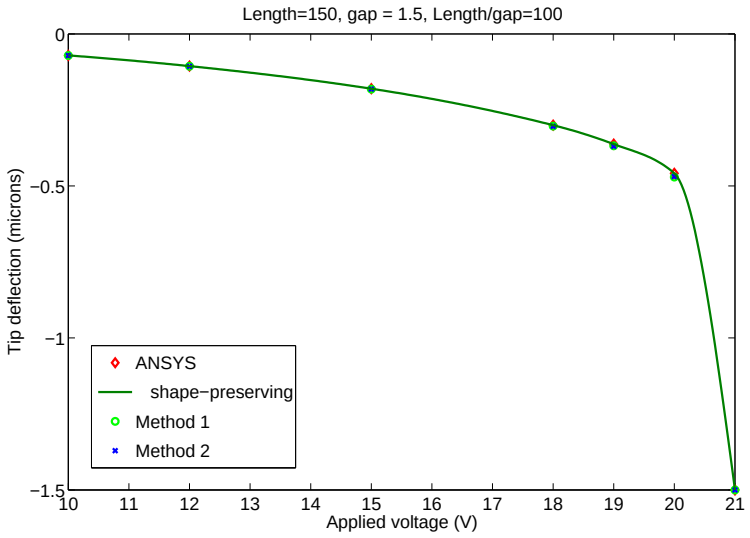

(a)

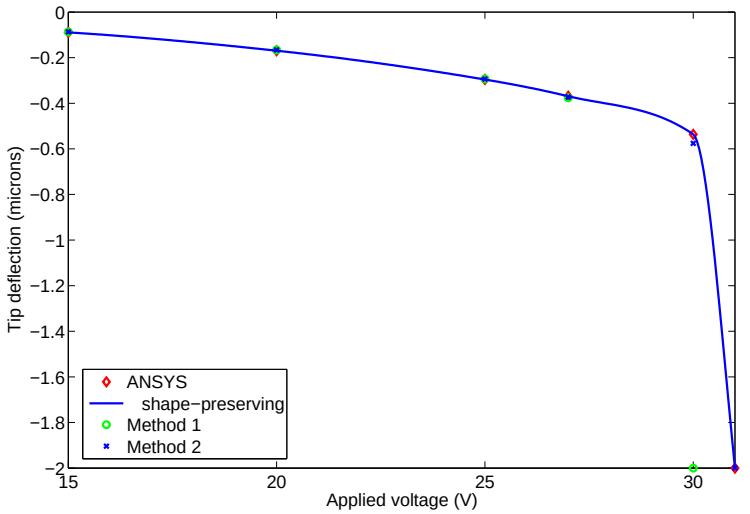

(b)

Figure 6. Tip deflection of cantilever : (a) gap length= 1.5 μm (b) gap length= 2 μm

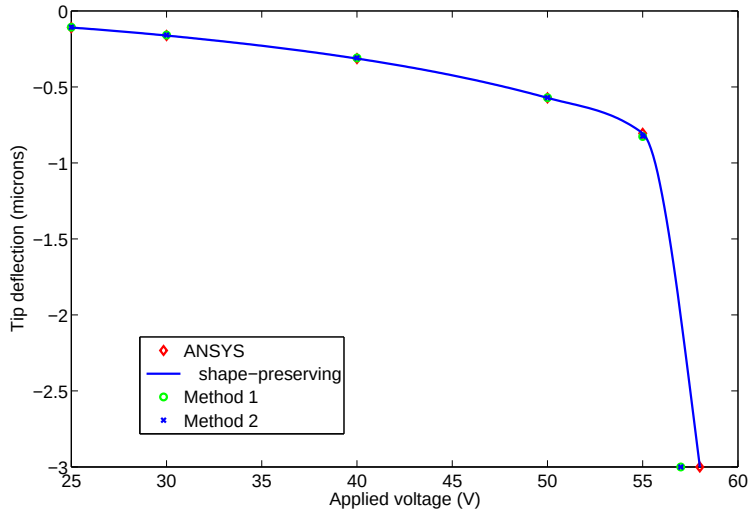

(a)

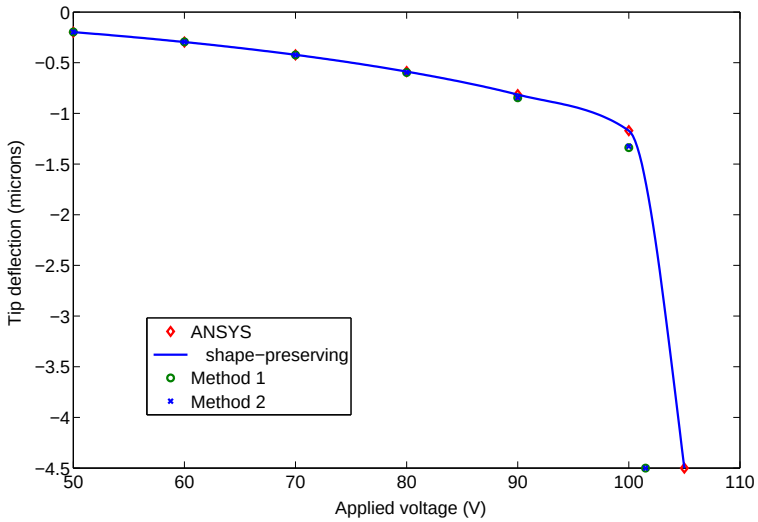

(b)

Figure 7. Tip deflection of cantilever : (a) gap length= 3.0 μm (b) gap length= 4.5 μm

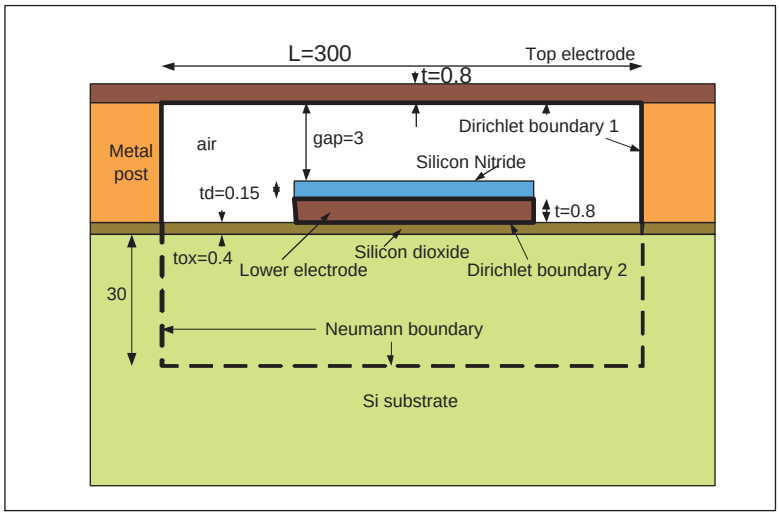

Figure 8. RF MEMS switch. All dimensions in microns.

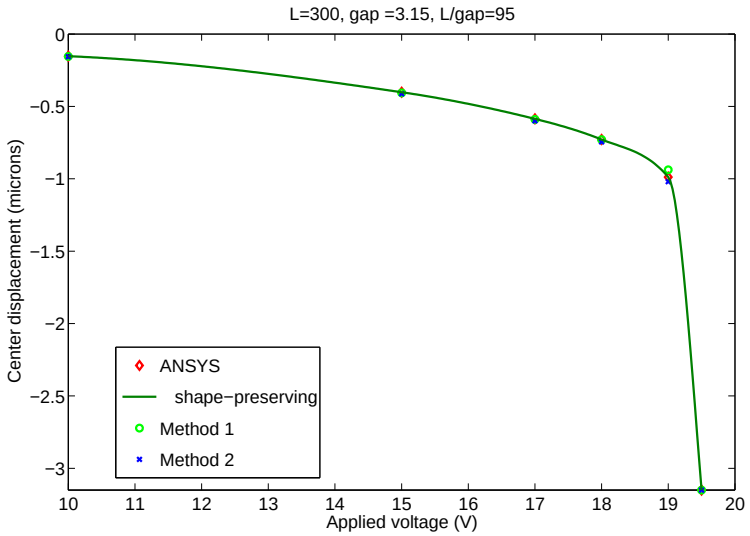

(a)

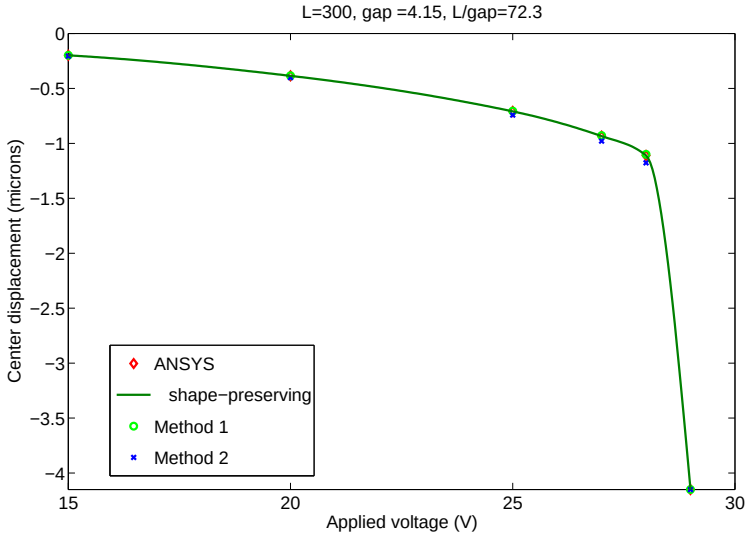

(b)

Figure 9. Center deflection of RF MEMS capacitive switch : (a) gap length= 3.15 μm (b) gap length= 4.15 μm

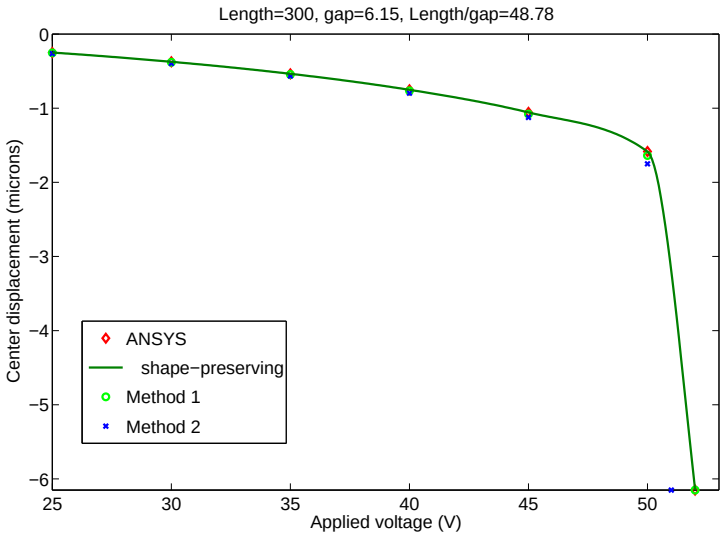

(a)

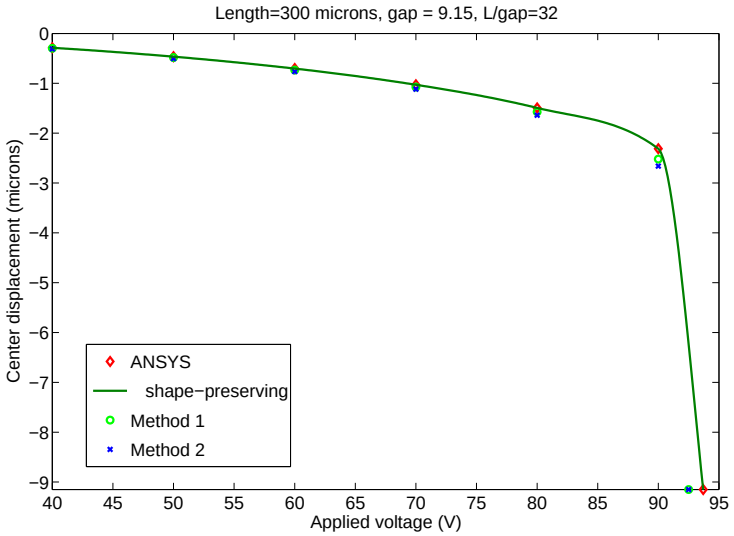

(b)

Figure 10. Center deflection of RF MEMS capacitive switch : (a) gap length= 6.15 μm (b) gap length= 9.15 μm

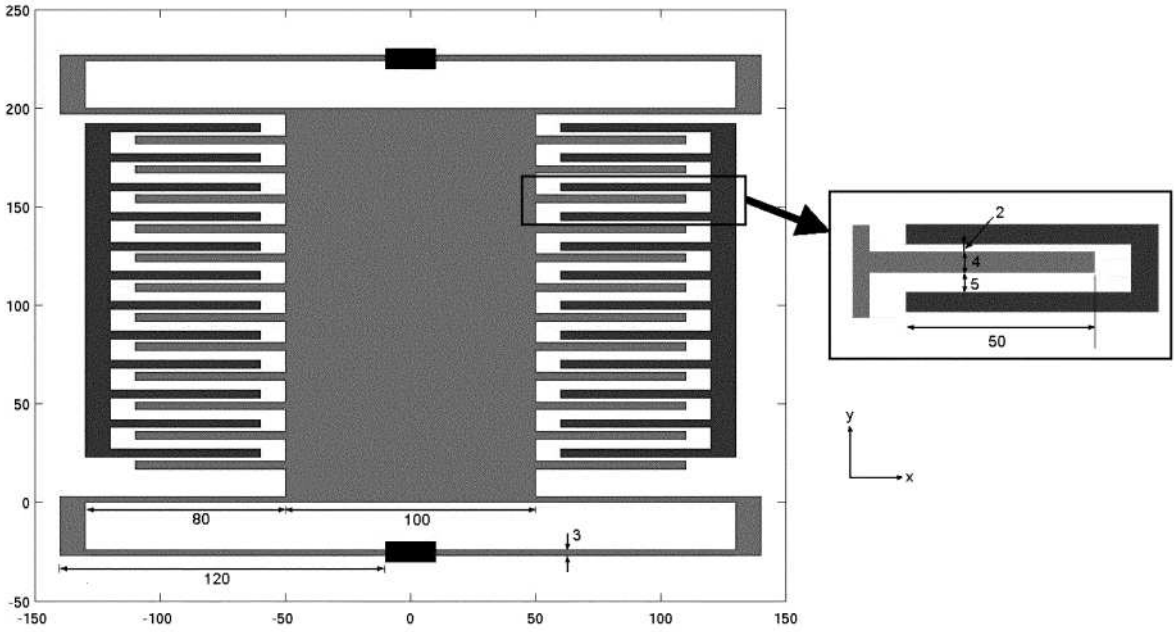

(a)

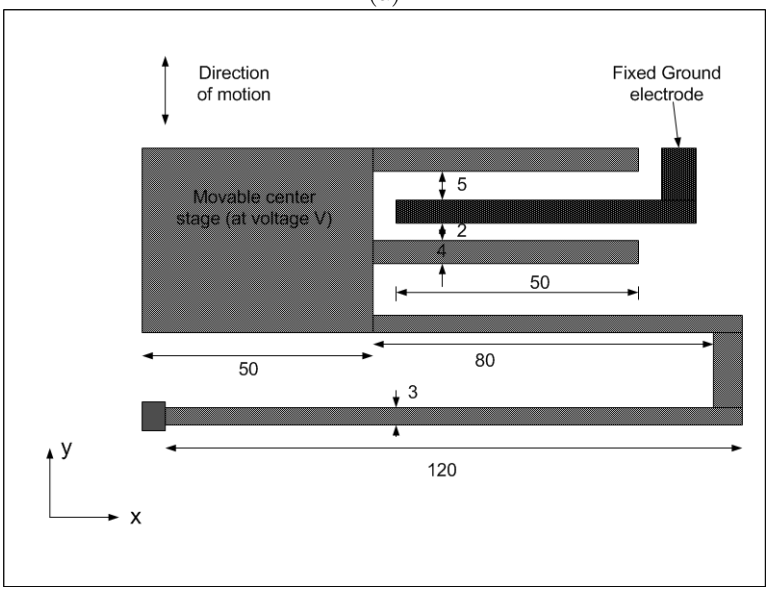

(b)

Figure 11. Comb drive (a) Actual design (b) Modeled geometry. All dimensions in microns.

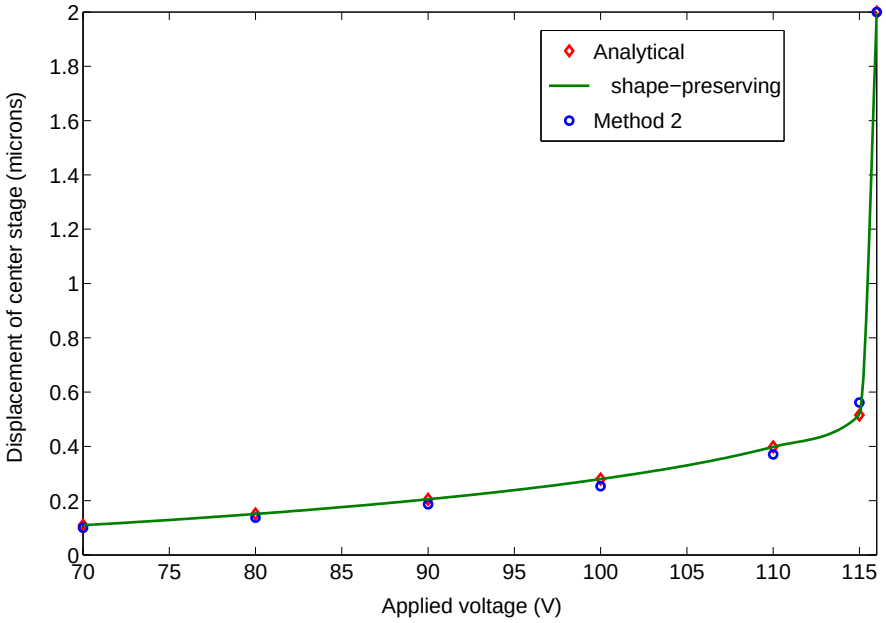

Figure 12. Transverse comb drive : comparison with analytical solution

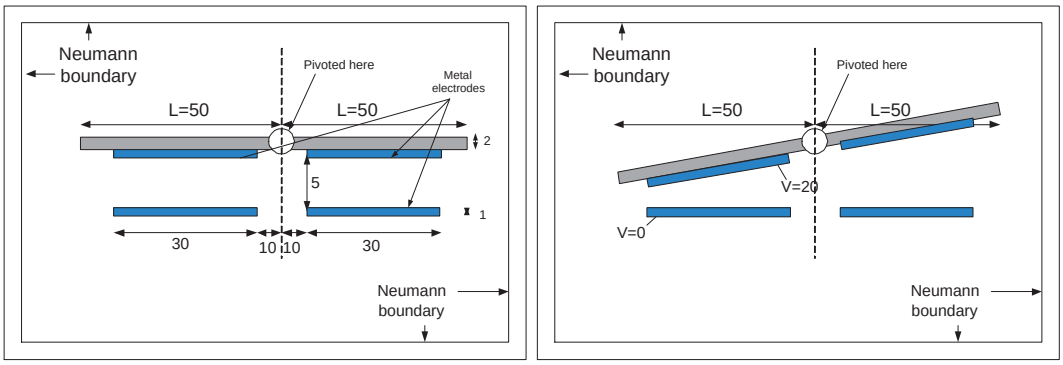

Figure 13. Torsion micro mirror (a) Undeformed state (b) Deformed state. All dimensions in microns.

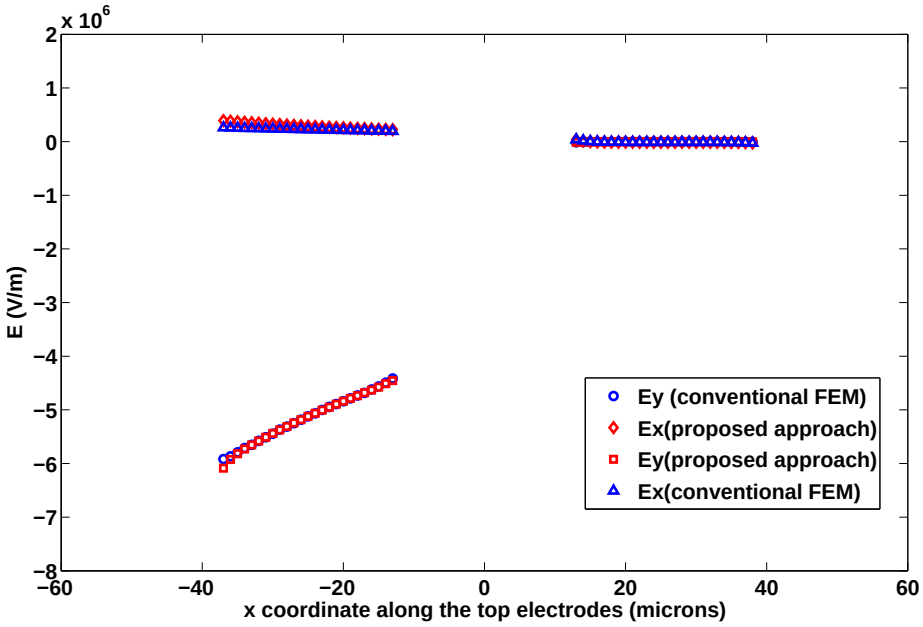

(a)

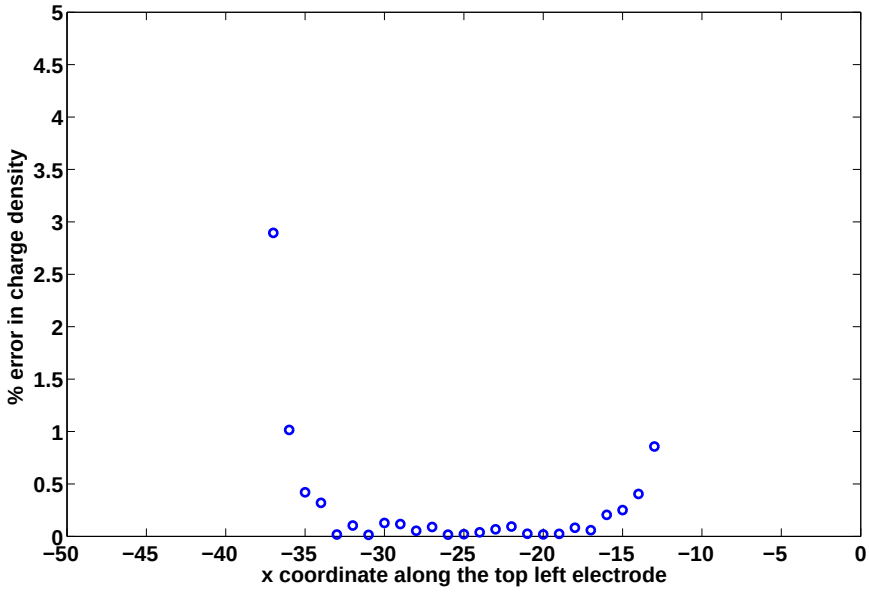

(b)

Figure 14. Torsion micro mirror electrostatic analysis: (a) Electric field comparison with conventional FEM (b) % error in charge density along the top left electrode.